

Gigabar Spherical Shock Generation on the OMEGA Laser

Recently it has been shown^{1–7} that the gain of an inertial confinement fusion implosion can be significantly enhanced by launching a strong spherically convergent shock at the end of the compression (or assembly) pulse. This two-step scheme is usually referred to as shock ignition (SI). Shock ignition has a distinct advantage over fast ignition⁸ because it reduces the energy required for ignition as compared to conventional hot-spot ignition⁹ while still using a single laser. Recent two-dimensional (2-D) simulations^{3,10} have indicated the possibility of achieving ignition at submegajoule laser energies. While implosion experiments on the OMEGA laser¹¹—using 60-beam symmetric implosions of CH shells filled with D₂—have demonstrated a fourfold increase in yield and a 40% increase in shell areal density for SI pulse shapes when compared to conventional implosions,¹² the final shock strength was much lower than the value required for ignition.

Demonstrating the capability to generate shocks of the order of ≥ 300 Mbar at laser intensities in the range of 10^{15} to 10^{16} W/cm² is crucial to the long-term success of SI. Investigations to determine the shock strength in planar geometries have been completed at Laboratoire pour l'Utilisation des Lasers Intenses (LULI),¹³ OMEGA,¹⁴ and Prague Asterix Laser System (PALS),¹⁵ where the largest shock pressure reported is ~ 90 Mbar at intensities $< 10^{16}$ W/cm². Kritcher *et al.*¹⁶ numerically investigated probing the equation of state of plastic under hundreds of megabar pressures in a spherical geometry using indirect-drive targets; however, current indirect-drive experiments at the National Ignition Facility (NIF)¹⁷ limit the ablation pressure to ~ 130 Mbar (Ref. 18).

This article reports on the first shock and ablation pressures inferred in spherical geometry using an x-ray flash as the primary diagnostic. The targets were composed of 430- to 600- μm -outer-diam solid spheres of 5% titanium-doped plastic in which the outer 50 μm consisted of pure CH (see Fig. 140.1). The targets were illuminated by a 2-ns laser pulse with a 1-ns, low-intensity foot used to create a coronal plasma followed by a 1-ns, high-intensity square pulse with 22 to 27 kJ of laser energy. An assortment of small phase plates¹⁹ were used to

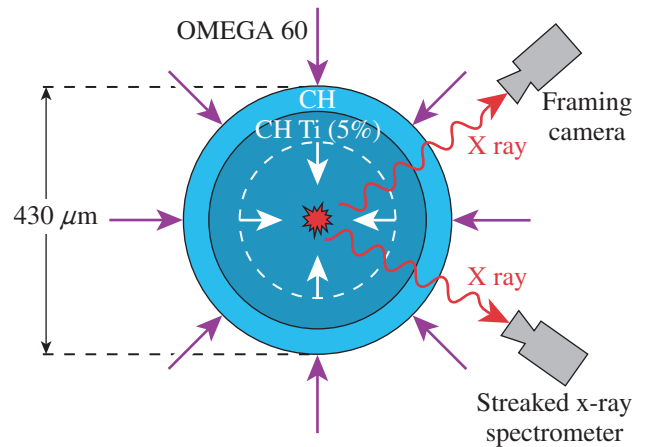
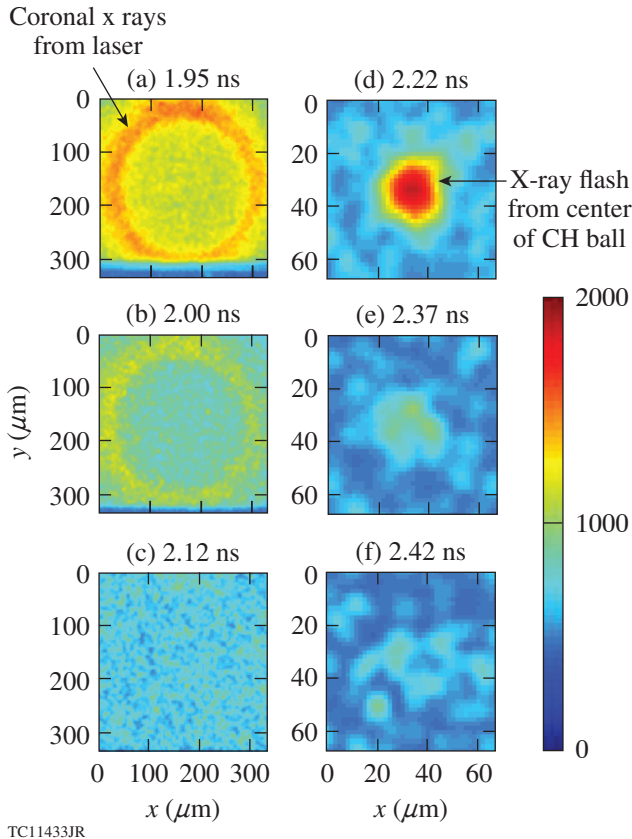


Figure 140.1
Experimental setup used to infer the shock and laser ablation pressure at shock-ignition (SI)-relevant intensities.

increase the on-target incident intensity up to $\sim 6 \times 10^{15}$ W/cm² at the initial target surface, both with and without smoothing by spectral dispersion (SSD).²⁰ The rapid rise in laser intensity by the high-intensity square pulse generated an inwardly propagating shock wave that converged at the center of the target, raising the temperature in a very small volume to hundreds of eV and resulting in the self-emission of x rays in the keV range. The seed shock pressure is inferred from hydrodynamic simulations constrained by the measured temporal occurrence of the x-ray flash.

The x-ray emission from the center of the target was resolved temporally, spatially, and spectrally using an x-ray framing camera (XRFC)²¹ and a streaked x-ray spectrometer (SXS).²² The XRFC spatially and temporally resolved the x-ray emission, using a 4×4 pinhole array to produce 16 enlarged images of the target on a microchannel-plate (MCP) detector, which was covered with four strips of gold film. A 200- μm Be foil and a thin (12- μm) Ti foil placed in front of the detector, combined with the spectral response of the diagnostic, restricted the range of recorded x rays to ~ 3 to 7 keV. Figure 140.2 shows a portion of the raw data collected with the XRFC for a typical experi-



TC11433JR

Figure 140.2

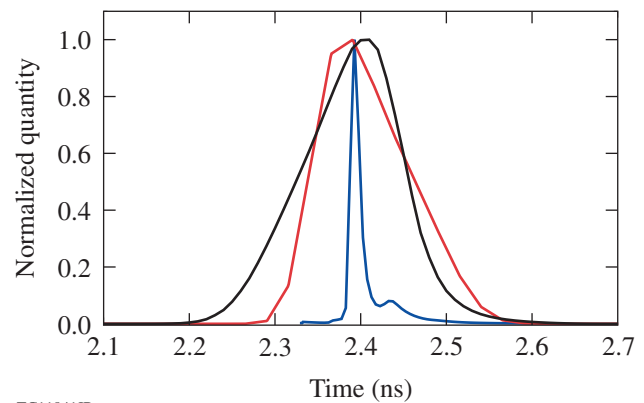
An x-ray framing camera (XRFC) captured a short x-ray flash at the time the shock converged in the center. The timing in each frame gives the peak time of the electrical gating pulse relative to the start of the laser pulse.

ment. At early times, the observed emission comes from the hot corona when the laser is still interacting with the target and, as time progresses, the laser shuts off and the corona cools. After a brief period of time, the appearance of a small but bright source of x rays originating from the center of the target is observed. The x ray emission was measured from a very small region with a diameter of less than $\sim 15 \mu\text{m}$ [full width at half maximum (FWHM)]. The simultaneously operated SXS captured this line emission and determined the temporal width of the emitted intensity to be shorter than $\sim 50 \text{ ps}$. The temporal occurrence of the x-ray flash between the two detectors is within the absolute timing error of each other.

The algorithm used to extract the x-ray flash times is based on Ref. 23. It translates the images formed onto the film or charge-coupled device (CCD) into an accurate time when the shock converged at the center of the target. To understand how the image is formed onto the film or a CCD camera, a brief description of the operation of the XRFC diagnostic and its

MCP is provided. The XRFC consists of four independent strips that form an image onto a CCD camera when a voltage bias is applied to the MCP. X rays incident on the Au-coated photocathode ionize the atoms and if the voltage pulse is being applied, locally gates the photoelectrons down a single tube within the MCP, multiplying in number with a dependence on the applied voltage (which propagates across the strip). The electrons are accelerated by the applied voltage from the back of the MCP to the front of the phosphor plate and impact the phosphor plate, turning the electron energy back into visible light. This light is then imaged onto a film pack or CCD camera. Each strip contains its own voltage pulse that propagates across the length of the strip in $\sim 200 \text{ ps}$. The bottom strip is triggered first, and subsequent strips (moving up) trigger once the voltage pulse has traversed the previous strip. This gives XRFC images that are both spatially resolved (via the pinhole array) and temporally gated (via the propagating voltage pulses).

The electrical gain of the photoelectrons as they travel down a single tube of the MCP is determined by the applied local voltage from the voltage pulse. As pointed out in Ref. 23, the gain scales with the voltage to the ninth power, $G \sim V^9$, for standard MCP setups. After discussions with many experimentalists, the exponent of the voltage dependence was changed to be as small as 5 or as large as 13, depending on the desired result. Figure 140.3 shows the gain of the voltage strip (red curve), shifted so the maximum occurs at 2.39 ns. The voltage pulse used in the model is the average of four pulse tests and is unique to each strip and framing camera; it has $\sim 150\text{-ps}$



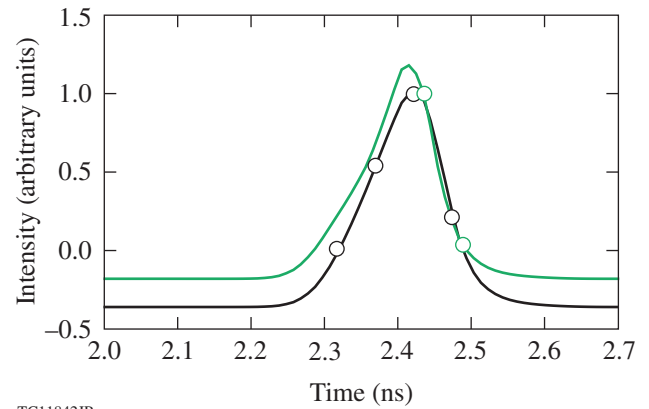
TC11841JR

Figure 140.3

Temporal profiles of the simulated x-ray emission intensity when the ignitor shock reaches the center of the target (blue curve), voltage gain triggering the collection of photons (red curve), and convolution of the red and blue curves (black curve) versus time. The convolution is used to fit the experimentally integrated x-ray signal from the XRFC to accurately determine the flash time.

FWHM. Also shown in Fig. 140.3 is the simulated x-ray emission as a function of time for a typical experiment, delineated as the blue curve. The temporal dependence of the x-ray emission was obtained from a *Spect3D*²⁴ post-processed *LILAC*²⁵ simulation and is averaged over the entire emission time and spectral range of 3 to 7 keV. Details of the radiation–hydrodynamic simulations are provided later. In the simulation, the ignitor shock reaches the center of the target at 2.390 ± 0.005 ns, resulting in the spike in x-ray emission. The emission decays after the shocked core cools and expands until a rebound shock causes a temporary increase in the emission. This secondary x-ray emission, however, is an order of magnitude weaker than the original x-ray emission; consequently, the FWHM of the simulated x-ray flash is ~ 15 ps. The convolution of the gain signal (red curve) and the simulated x-ray emission (blue curve) in Fig. 140.3 predicts the experimental intensity of the x-ray flash as a function of time (black curve). This indicates the x-ray emission would follow the shape of the convolution as a function of time and is used to translate the experimentally integrated pinhole images from XRFC into a specific x-ray flash time.

The signal gain of each strip (and camera) is convolved with the simulated x-ray emission, and its shape is compared to the experimentally measured intensity for each shot to determine the x-ray flash time. The intensity of the x-ray emission from each frame of the XRFC data is spatially integrated over the entire emission of a single pinhole image. The background emission from the cooling coronal plasma is subtracted from the integrated image and a low-pass filter is applied to the resulting data. The signal strength from each pinhole image is then fit to a Gaussian distribution and compared to the strength of the other images on the same strip. The relative values of these images are then compared to the simulated x-ray emission intensity to infer the x-ray flash time. Figure 140.4 shows the convolution of the voltage pulse gain from strips 2 and 3 (black and green curves, respectively) from XRFC4 for shot 72673 and compares it to the experimental intensity from that shot (circles). The spacing between each experimental point (circle) is determined by the time it takes the voltage pulse to propagate from one frame to another; it can be seen that the third and fourth frames of the second strip occur at roughly the same time as the first and second frames of the third strip. Because the voltage gain is unique to each strip, this analysis does not compare the signal strengths between strips but compares only the relative signal strength within the same strip. In Fig. 140.4, the convolutions have been adjusted in height and vertical offset to obtain the best fit of the experimental data to determine the x-ray flash time.



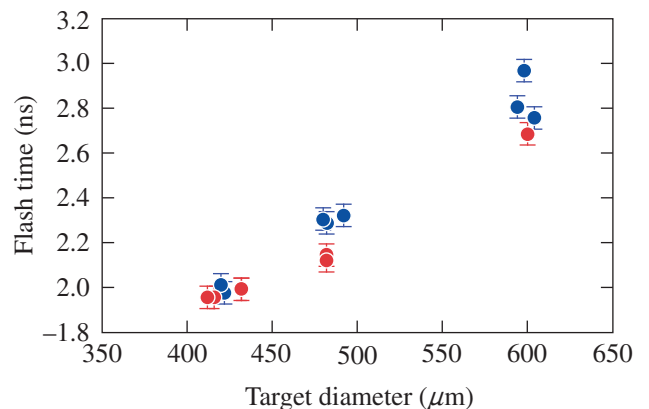
TC11842JR

Figure 140.4

Best fit of the XRFC model used to extract the x-ray flash time from the data for shot 72673. The convolutions of the voltage pulse with the simulated x-ray emission are shown for strip 2 (black curve) and strip 3 (green curve) versus absolute time. The circles indicate the strip-normalized integrated intensity of the measured x-ray emission for each pinhole image.

The flash-time extraction analysis was applied to all of the experiments throughout the campaign, and the result of this analysis is shown in Fig. 140.5. A clear correlation between the size of the target and when the x-ray flash occurs is clearly observed, with smaller targets exhibiting earlier flash times. Also shown is the effect turning SSD on (blue) or off (red) has on the x-ray flash time. Generally, it is observed that experiments operating without SSD had earlier x-ray flash times because of the much larger amounts of generated suprathermal electrons.

Copious amounts of suprathermal electrons are generated when the thresholds for two-plasmon–decay (TPD) and stimu-



TC11843JR

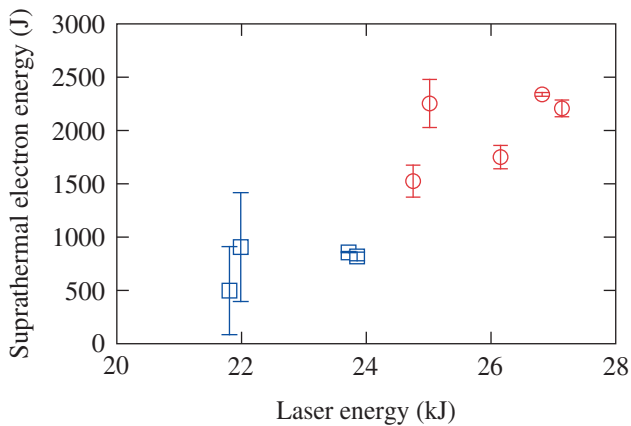
Figure 140.5

Experimental x-ray flash time versus target diameter for shots with SSD (blue) and without SSD (red). The error bars signify the ± 50 -ps accuracy in the absolute timing of the diagnostics.

lated Raman scattering (SRS) instabilities are exceeded early during the rise of the high-intensity square pulse.²⁶ The temperature of the suprathermal electrons and the temporal dependence were measured with a time-resolved, four-channel hard x-ray detector (HXRD)²⁷ and two time-integrated imaging-plate diagnostics—high-energy-radiography imager (HERIE)²⁸ and bremsstrahlung x-ray spectrometer (BMXS).²⁹ Typical temperatures measured for the suprathermal electrons can be fit to single-temperature Maxwellian distributions with central temperatures in the range of 50 to 100 keV. Up to 2 kJ (~8% of the total incident laser energy and 15% instantaneously) of suprathermal electrons were inferred to be deposited into the target by comparing the measured bremsstrahlung emission to Monte Carlo simulations, assuming that the suprathermal electrons were generated isotropically. Figure 140.6 shows that the measured total energy of the suprathermal electrons increased with the total laser energy and was dependent on whether or not SSD was functioning. The integrated intensity of the x-ray emission from shock convergence was measured with a gated microscope x-ray imager (GMXI)³⁰ and found to experience an ~25× increase when SSD was not operating (more suprathermal electrons) as compared to the case when SSD was turned on, indicating that the strength of the shock is greatly enhanced by the hot electrons. Measured time-resolved spectra for SRS, $\omega/2$, and $3\omega/2$ emissions show that both TPD and SRS are active. The observation of moderate suprathermal electron temperatures at these laser intensities has a significant

impact on SI designs since they can enhance the ignitor shock³¹ and improve the implosion performance.¹⁰

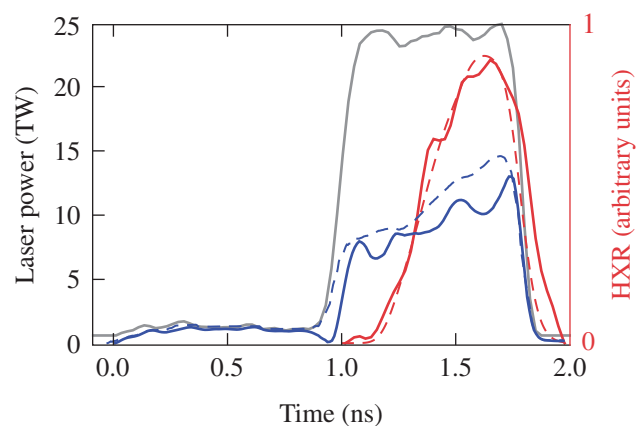
The shock and ablation pressures are inferred by constraining radiation–hydrodynamic simulations to the experimental observables: the temporal occurrence of the x-ray emission, the suprathermal electron energy and temperature distribution, and the temporal evolution of the hard x-ray emission (see Fig. 140.7). The simulations used the radiation–hydrodynamic code *LILAC* and were run with a multigroup radiation diffusion model, Thomas–Fermi³² or *SESAME*^{33,34} equations of state (EOS), flux-limited thermal transport,³⁵ and a suprathermal electron-transport package.³⁶ The suprathermal electron-transport package is a straight-line deposition model whereby a fraction of the laser energy reaching the quarter-critical surface is converted into suprathermal electrons with a single-temperature Maxwellian distribution and 2π forward divergence. The stopping range of the suprathermal electrons is modeled via collisional effects and is computed based on the work by Solodov and Betti.³⁷ The flux limiter, which is the only free parameter within the radiation–hydrodynamic simulations, is adjusted to match the experimentally measured x-ray flash time. Each simulation is, in principle, constrained by its own x-ray flash time and, therefore, has a unique flux limiter ranging from 5% to 8%; however, choosing 6.5% constrains all of the simulations within the experimental error bars. The ablation pressure is the pressure in the shell at the position where the



TC11434JR

Figure 140.6

Total energy converted into suprathermal electrons versus laser energy. Up to ~8% of the total laser energy was converted into suprathermal electrons at moderate temperatures (50 to 100 keV). The error bars represent half the high-energy-radiography imager (HERIE) and bremsstrahlung x-ray spectrometer (BMXS) differences between the two time-integrated imaging-plate diagnostics.



TC11435JR

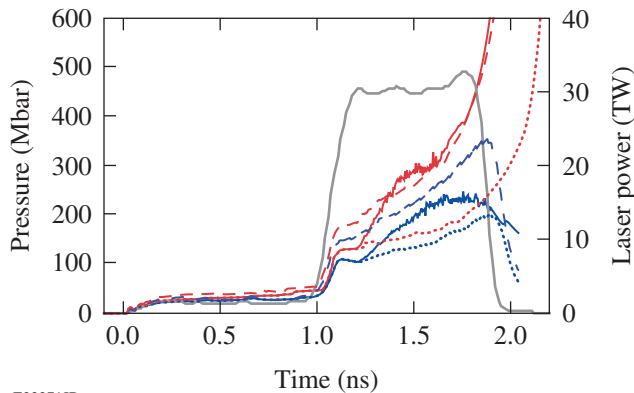
Figure 140.7

Comparison of a typical experimental (solid curves) and simulated (dashed curves) incident laser power (gray curves), laser absorption (blue curves), and hard x-ray emission (HXR, red curves) resulting from suprathermal electrons (in arbitrary units). The experimental hard x-ray emission was averaged over the three highest HXRD channels.

material velocity is zero in the lab frame, an accurate approximation for slowly imploding solid spheres.

Figure 140.8 illustrates the shock and ablation pressure inferred from a typical simulation that matches all of the experimental observables. The ablation pressure (blue curves) increases as a function of time, resulting from both thermal conduction of the absorbed laser energy and the energy deposition by suprathermal electrons, and decays soon after the laser is shut off. Meanwhile, the shock pressure (red curves) rapidly increases in time because of convergence effects.³⁸ For the particular shot shown in Fig. 140.8, the shock pressure is inferred to exceed 1 Gbar when the shock is $\sim 25 \mu\text{m}$ from the center of the target. Additionally, simulations including suprathermal electrons (solid curves in Fig. 140.8) are observed to significantly enhance the ablation pressure by up to $\sim 50\%$ instantaneously over the case when the simulation is repeated in the absence of suprathermal electrons (dotted curves in Fig. 140.8). This result is corroborated with recent theoretical work showing $\sim 300\text{-Mbar}$ shock pressures can be generated solely by suprathermal electrons.^{39,40}

Inspection of Fig. 140.8 illustrates that a significant fraction of the energy carried by suprathermal electrons is deposited beyond the ablation front and contributes to the overall shock strength. In this specific example at 1.6 ns, only suprathermal electrons with temperatures less than 60 keV are stopped before



E23271JR

Figure 140.8
Simulated ablation pressure (blue curves) and shock pressure (red curves) as a function of time for shot 72679. The solid lines indicate a simulation that matches all experimentally observed quantities using a flux limiter of 5%. The dotted lines are the simulation results in the absence of suprathermal electrons (flux limiter of 5%). The dashed lines indicate a simulation that also matches the x-ray flash time but in the absence of suprathermal electrons (the flux limiter was increased to 8%). For reference, the solid gray line indicates the laser pulse.

the ablation surface, corresponding to $\sim 12\%$ of the total energy in a 70-keV Maxwellian distribution, while suprathermal electrons with temperatures from 60 to 200 keV are stopped between the ablation and shock front, corresponding to $\sim 55\%$ of the total suprathermal energy. Therefore, using the ablation pressure as a metric to describe the conversion of laser energy into a shock strength is no longer valid. A more-effective metric in this case would be to adjust the energy transport model to simulate the effect of suprathermal electrons on the shock strength and observe a new “effective ablation pressure.” The effective ablation pressure (dashed curves in Fig. 140.8) drives the shock at the same velocity as when suprathermal electrons are included (solid curves in Fig. 140.8) but without the use of suprathermal electrons. This is achieved by increasing the flux limiter and is unique to each shot in the campaign. Physically, this can be explained by the fact that a shock must travel from the outside of the target to the center in the measured period of time regardless of how the energy is transferred. Therefore, whether the shock is solely driven by the rocket effect or by a combination of ablation pressure and suprathermal-electron energy deposition, the pressure behind the shock must be independent of the mechanism driving the shock and even insensitive of many physics details. Corroborating this point is the choice of equation of state (EOS); whether using Thomas–Fermi or *SESAME*, the resulting shock pressure required to match the experimental observables remains the same despite differences in post-shock mass density. The ambiguity in EOS could be solved by a direct measurement of the mass density (e.g., Ref. 16).

It was found that the maximum ablation pressure P_a^{\max} and effective maximum ablation pressure P_a^{eff} for all of the experiments scale with the absorbed laser intensity at the critical surface, $I_{15 \text{ abs}}$, in units of 10^{15} W/cm^2 via the following formulas:

$$P_a^{\max} (\text{Mbar}) \approx 90 I_{15 \text{ abs}}^{1.2}, \quad (1)$$

$$P_a^{\text{eff}} (\text{Mbar}) \approx 90 I_{15 \text{ abs}}^{1.4}, \quad (2)$$

and are shown in Fig. 140.9. The error bars in Fig. 140.9 are the result of adjusting the simulated x-ray flash time by $\pm 50 \text{ ps}$ as a result of the absolute error in the timing diagnostics, changing both the simulated absorbed intensity and ablation pressure. This scaling shows a significant departure from previous spherical ablation pressure scaling $P_a^{\text{theory}} \approx 100 I_{15 \text{ abs}}^{7/9}$, derived for low intensities ($\leq 10^{15} \text{ W/cm}^2$) (Ref. 41). The differences are likely caused by the much larger laser intensities being used as well as the presence of copious amounts of

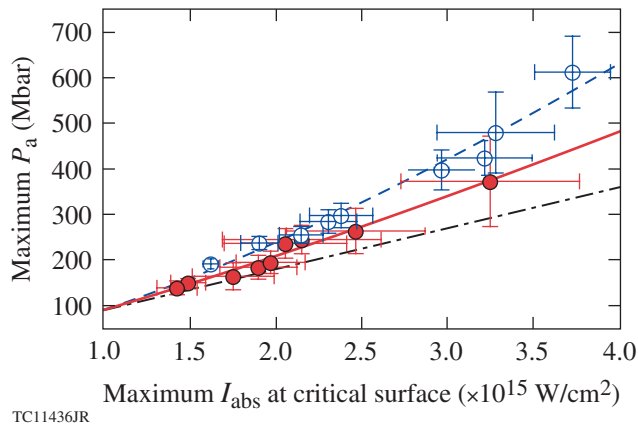


Figure 140.9

Scaling of the inferred maximum ablation pressure with suprathermal electrons (solid red circles and solid line) and effective maximum ablation pressure without suprathermal electrons (open blue circles and dashed line) versus the maximum laser intensity that is absorbed at the critical surface for simulations matching all of the experimental observables. The dashed-dotted line indicates the linear dependence of the ablation pressure on the absorbed laser intensity for unconstrained simulations with a flux limiter value of 6.5%.

suprathermal electrons that enhance the ablation pressure. An analysis of simulations in the absence of suprathermal electrons determined that the exponent of the ablation pressure scaling varies with the choice of flux limiter, e.g., choosing a value of 6.5% yields a linear dependence on the absorbed laser intensity (black dashed-dotted curve in Fig. 140.9). Comparing this curve with Eq. (1) demonstrates how suprathermal electrons enhance the ablation pressure.

Extrapolating Eqs. (1) and (2) to the absorbed laser intensities of $\sim 7 \times 10^{15} \text{ W/cm}^2$ used in the 700-kJ NIF SI point design of Ref. 10, one finds ablation pressures that significantly exceed the required $\sim 600 \text{ Mbar}$ (0.9 Gbar and 1.3 Gbar, respectively), indicating predicted ablation pressures to be high enough for robust ignition. However, NIF-scale ignition targets are much larger than those used in these OMEGA experiments, thereby leading to longer-scale-length plasmas at the time of shock launch. Higher levels of laser-plasma instabilities are expected, and a simple extrapolation of Eqs. (1) and (2) to NIF-scale plasmas may not be applicable. Therefore, despite these encouraging results obtained on OMEGA, an accurate extrapolation of the shock pressure to NIF requires experiments on NIF-scale targets.

In summary, this article reports on the first experimental ablation-pressure inferences in spherical geometries at SI-relevant laser intensities. Up to 8% of the laser energy was

converted into suprathermal electrons that enhanced both the ablation pressure driving the shock and the shock itself, leading to an inferred effective ablation pressure scaling with the absorbed laser intensity of $P_a^{\text{eff}} (\text{Mbar}) \approx 90 I_{15\text{abs}}^{1.4}$. This result demonstrates the ability to launch several-hundred-Mbar shocks at SI-relevant laser intensities with the generation of moderate-temperature suprathermal electrons.

ACKNOWLEDGMENT

This material is based upon work supported by the Department of Energy National Nuclear Security Administration under Award Number DE-NA0001944, the Office of Fusion Energy Sciences Number DE-FG02-04ER54786, the University of Rochester, and the New York State Energy Research and Development Authority. The support of DOE does not constitute an endorsement by DOE of the views expressed in this article.

REFERENCES

1. R. Betti, C. D. Zhou, K. S. Anderson, L. J. Perkins, W. Theobald, and A. A. Solodov, *Phys. Rev. Lett.* **98**, 155001 (2007).
2. L. J. Perkins, R. Betti, K. N. LaFortune, and W. H. Williams, *Phys. Rev. Lett.* **103**, 045004 (2009).
3. X. Ribeyre, G. Schurtz, M. Lafon, S. Galera, and S. Weber, *Plasma Phys. Control. Fusion* **51**, 015013 (2009).
4. M. Lafon, X. Ribeyre, and G. Schurtz, *Phys. Plasmas* **20**, 022708 (2013).
5. A. J. Schmitt *et al.*, *Phys. Plasmas* **17**, 042701 (2010).
6. S. Atzeni, X. Ribeyre, G. Schurtz, A. J. Schmitt, B. Canaud, R. Betti, and L. J. Perkins, *Nucl. Fusion* **54**, 054008 (2014).
7. D. Batani, S. Baton, A. Casner, S. Depierreux, M. Hohenberger, O. Klimo, M. Koenig, C. Labaune, X. Ribeyre, C. Rousseaux, G. Schurtz, W. Theobald, and V. Tikhonchuk, *Nucl. Fusion* **54**, 054009 (2014).
8. M. Tabak *et al.*, *Phys. Plasmas* **1**, 1626 (1994).
9. J. Nuckolls *et al.*, *Nature* **239**, 139 (1972).
10. K. S. Anderson, R. Betti, P. W. McKenty, T. J. B. Collins, M. Hohenberger, W. Theobald, R. S. Craxton, J. A. Delettrez, M. Lafon, J. A. Marozas, R. Nora, S. Skupsky, and A. Shvydky, *Phys. Plasmas* **20**, 056312 (2013).
11. T. R. Boehly, D. L. Brown, R. S. Craxton, R. L. Keck, J. P. Knauer, J. H. Kelly, T. J. Kessler, S. A. Kumpan, S. J. Loucks, S. A. Letzring, F. J. Marshall, R. L. McCrory, S. F. B. Morse, W. Seka, J. M. Soares, and C. P. Verdon, *Opt. Commun.* **133**, 495 (1997).
12. W. Theobald, R. Betti, C. Stoeckl, K. S. Anderson, J. A. Delettrez, V. Yu. Glebov, V. N. Goncharov, F. J. Marshall, D. N. Maywar, R. L. McCrory, D. D. Meyerhofer, P. B. Radha, T. C. Sangster, W. Seka, D. Shvarts, V. A. Smalyuk, A. A. Solodov, B. Yaakobi, C. D. Zhou, J. A. Frenje, C. K. Li, F. H. Séguin, R. D. Petrasso, and L. J. Perkins, *Phys. Plasmas* **15**, 056306 (2008).

13. S. D. Baton *et al.*, Phys. Rev. Lett. **108**, 195002 (2012).
14. M. Hohenberger, W. Theobald, S. X. Hu, K. S. Anderson, R. Betti, T. R. Boehly, A. Casner, D. E. Fratanduono, M. Lafon, D. D. Meyerhofer, R. Nora, X. Ribeyre, T. C. Sangster, G. Schurtz, W. Seka, C. Stoeckl, and B. Yaakobi, Phys. Plasmas **21**, 022702 (2014).
15. D. Batani *et al.*, Phys. Plasmas **21**, 032710 (2014).
16. A. L. Kritcher *et al.*, High Energy Density Phys. **10**, 27 (2014).
17. G. H. Miller, E. I. Moses, and C. R. Wuest, Opt. Eng. **43**, 2841 (2004).
18. J. D. Lindl, Phys. Plasmas **2**, 3933 (1995).
19. S. P. Regan, T. C. Sangster, D. D. Meyerhofer, W. Seka, R. Epstein, S. J. Loucks, R. L. McCrory, C. Stoeckl, V. Yu. Glebov, O. S. Jones, D. A. Callahan, P. A. Amendt, N. B. Meezan, L. J. Suter, M. D. Rosen, O. L. Landen, E. L. DeWald, S. H. Glenzer, C. Sorce, S. Dixit, R. E. Turner, and B. MacGowan, J. Phys.: Conf. Ser. **112**, 022077 (2008).
20. S. Skupsky, R. W. Short, T. Kessler, R. S. Craxton, S. Letzring, and J. M. Soures, J. Appl. Phys. **66**, 3456 (1989).
21. D. K. Bradley, P. M. Bell, J. D. Kilkenny, R. Hanks, O. Landen, P. A. Jaanimagi, P. W. McKenty, and C. P. Verdon, Rev. Sci. Instrum. **63**, 4813 (1992).
22. M. Millecchia, S. P. Regan, R. E. Bahr, M. Romanofsky, and C. Sorce, Rev. Sci. Instrum. **83**, 10E107 (2012).
23. D. K. Bradley, P. M. Bell, J. D. Kilkenny, R. Hanks, O. Landen, P. A. Jaanimagi, P. W. McKenty, and C. P. Verdon, Rev. Sci. Instrum. **63**, 4813 (1992).
24. J. J. MacFarlane *et al.*, in *Inertial Fusion Sciences and Applications 2003*, edited by B. A. Hammel, D. D. Meyerhofer, J. Meyer-ter-Vehn, and H. Azechi (American Nuclear Society, La Grange Park, IL, 2004), pp. 457–460.
25. E. Goldman, Laboratory for Laser Energetics, University of Rochester, Rochester, NY, LLE Report No. 16 (1973).
26. J. F. Myatt, J. Zhang, R. W. Short, A. V. Maximov, W. Seka, D. H. Froula, D. H. Edgell, D. T. Michel, I. V. Igumenshchev, D. E. Hinkel, P. Michel, and J. D. Moody, Phys. Plasmas **21**, 055501 (2014).
27. C. Stoeckl, V. Yu. Glebov, D. D. Meyerhofer, W. Seka, B. Yaakobi, R. P. J. Town, and J. D. Zuegel, Rev. Sci. Instrum. **72**, 1197 (2001).
28. R. Tommasini *et al.*, Rev. Sci. Instrum. **77**, 10E301 (2006).
29. C. D. Chen *et al.*, Rev. Sci. Instrum. **79**, 10E305 (2008).
30. F. J. Marshall and J. A. Oertel, Rev. Sci. Instrum. **68**, 735 (1997).
31. R. Betti, W. Theobald, C. D. Zhou, K. S. Anderson, P. W. McKenty, S. Skupsky, D. Shvarts, V. N. Goncharov, J. A. Delettrez, P. B. Radha, T. C. Sangster, C. Stoeckl, and D. D. Meyerhofer, J. Phys.: Conf. Ser. **112**, 022024 (2008).
32. A. R. Bell, Rutherford Appleton Laboratory, Chilton, Didcot, Oxon, England, Report RL-80-091 (1980).
33. G. I. Kerley, Phys. Earth Planet. Inter. **6**, 78 (1972).
34. G. I. Kerley, Sandia National Laboratory, Albuquerque, NM, Report SAND2003-3613 (2003).
35. R. C. Malone, R. L. McCrory, and R. L. Morse, Phys. Rev. Lett. **34**, 721 (1975).
36. J. Delettrez and E. B. Goldman, Laboratory for Laser Energetics, University of Rochester, Rochester, NY, LLE Report No. 36 (1976).
37. A. A. Solodov and R. Betti, Phys. Plasmas **15**, 042707 (2008).
38. Von G. Guderley, Luftfahrtforschung **19**, 302 (1942).
39. S. Gus'kov *et al.*, Phys. Rev. Lett. **109**, 255004 (2012).
40. X. Ribeyre *et al.*, Phys. Plasmas **20**, 062705 (2013).
41. S. Atzeni, Plasma Phys. Control. Fusion **42**, B143 (2000).